

Anisotropic equal-spin Andreev reflection and spin-triplet pairing correlations in antiferromagnet/antiferromagnet/superconductor junctions

Lu Ming Cai ¹ and Zhi Ping Niu ^{1,2,*}

¹College of Physics, Nanjing University of Aeronautics and Astronautics, Nanjing 211106, China

²Key Laboratory of Aerospace Information Materials and Physics (NUAA), MIIT, Nanjing 211106, China



(Received 19 March 2024; revised 6 June 2024; accepted 25 June 2024; published 8 July 2024)

We theoretically study Andreev reflection (AR)-induced conductance at antiferromagnet/antiferromagnet/superconductor (AF/AF/S) junctions. The AF can become spin-polarized when the parity-time symmetry is broken. Equal-spin AR occurs due to spin-flip scattering when the Néel vectors of the AFs are noncollinear. We investigate how the staggered sublattice potential and the electrostatic potential affect the AR-induced conductance, and we demonstrate that a pure equal-spin AR is achievable. The signature of the equal-spin AR can be confirmed by studying the conductance spectra. When the left AF is fully spin-polarized, the pairing correlations involving spin-down quasiparticles decrease rapidly, but the equal-spin triplet pairing correlation ($\uparrow\uparrow$) becomes long-range. This results in a conversion from spin-singlet to spin-triplet pairings, providing further evidence for the existence of equal-spin AR. Specifically, the study focuses on the AR-induced magnetoanisotropic conductance. The conductance exhibits relatively weak magnetoanisotropy due to the competing contributions of conventional and equal-spin ARs. In contrast, when only equal-spin AR is present, significant anisotropic magnetoresistance is observed, which can serve as a distinctive signature of equal-spin AR. The findings suggest that AF/S junctions are ideal platforms for future superconducting spintronics applications.

DOI: [10.1103/PhysRevB.110.014505](https://doi.org/10.1103/PhysRevB.110.014505)

I. INTRODUCTION

Andreev reflection (AR) is a scattering process that occurs at the metal-superconductor (S) interface [1–4]. When an electron is reflected as a hole at the metal-S contact, it creates a Cooper pair with a charge of $2e$ on the S side. At bias voltages below the superconducting gap, this process converts a conventional dissipative current into a dissipationless supercurrent. In ferromagnet (F)/S junctions with a homogeneous exchange field, conventional AR occurs when the incident electron and the Andreev-reflected hole are from different spin bands. The conventional AR has a strong influence on transport behavior, allowing for the experimental extraction of the spin polarization of the F [5]. Nevertheless, this conventional AR is easily destroyed by an exchange field as it involves both spin-up and spin-down quasiparticles. On the other hand, equal-spin AR is created through spin-flip scattering, in which the incident electron and the Andreev-reflected hole are from the same spin band. Inhomogeneous exchange fields in real-space [6–10] and/or spin-orbit fields in reciprocal-space [11–14] at engineered F/S interfaces have been investigated as potential sources of equal-spin AR. The signature of equal-spin AR can be identified through the conductance spectra [6–13]. For example, Linder and Sudbø [6] studied the signature of the equal-spin AR, or retroreflected holes with the same spin as the incoming electron, in an F/s-wave S junction. The conductance spectra of half-metallic F/s-wave S contacts should show zero-bias conductance vanishing, providing clear

evidence for the presence of equal-spin AR [7]. Costa and Fabian [11] investigated anisotropic magnetoresistance effects and spin-triplet pairs in F/S/F double-barrier junctions. Significant anisotropic magnetoresistance was observed at the interface between a quasi-two-dimensional van der Waals F and an *s*-wave S, providing potential experimental evidence for equal-spin AR [12]. Nevertheless, magnetic multilayers and the desired noncollinear alignment of their magnetization directions below the exchange length scales are rare and remain difficult to control, which makes controllable equal-spin AR difficult to generate experimentally.

On the other hand, superconducting spin-singlet pairing correlations can evolve into spin-triplets via spin mixing and spin-flip scattering processes at the F/S interface [15–29]. Superconducting spin-triplet pairing correlations have been predicted theoretically [16–20], and then much effort has been put into verifying their existence [21–29]. In contrast to spin-singlet pairings, which are limited by ferromagnetic polarization, equal-spin spin-triplet pairings can generate long-range Josephson coupling in the F that is immune to strong spin polarization, which is necessary for superconducting spintronics. Consequently, the spin-triplet pairings have been extensively studied experimentally using the Josephson current technique. For example, Keizer *et al.* [21] demonstrated the long-range Josephson supercurrent in NbTiN/CrO₂/NbTiN lateral Josephson devices. Equal-spin triplet superconductivity can also be created by introducing a thin Ni film into the CrO₂/S contact [27,29]. Furthermore, Manzano *et al.* [28] demonstrated a high-temperature spin-triplet Josephson supercurrent in YBCO/half-metal heterostructures. Evidence for long-range spin-triplet pairings in

*Contact author: zpnui@nuaa.edu.cn

these F/S junctions has been revealed through investigations into the dependence of the superconducting critical temperature on the magnetic state [29–33]. Spectroscopic evidence of spin-triplet states has been reported through the analysis of subgap states in the superconducting density of states [34–38]. Therefore, the existence of spin-triplet pairing correlations serves as another manifestation of equal-spin AR.

The interplay between antiferromagnetism and superconductivity has yielded fascinating phenomena in antiferromagnet (AF)/S hybrid structures [39–57]. Theoretical predictions suggest that AF/S junctions will exhibit unconventional AR and bound states [48–52]. For example, Jakobsen *et al.* [44] displayed a strong signal of perfect crossed AR in the nonlocal differential conductance of AF/S/AF junctions with hexagonal lattices. Yan *et al.* [45] investigated AR in graphene-based AF/F/S junctions and discovered that equal-spin AR can arise due to spin-flip scattering induced by the F. Rashba spin-orbit coupling in the normal layer at the AF/normal/S junctions can lead to equal-spin AR via spin-flip scattering [46]. The dc Josephson current across S/AF/S junctions typically exhibits short-range atomic scale $0-\pi$ transitions [51–57]. In particular, Rashba spin-orbit coupling is predicted to cause an anomalous supercurrent in AF Josephson junctions [53]. In contrast to previous work [51–57], Jeon *et al.* [41] discovered a spin-polarized long-range supercurrent in a topological noncollinear S/AF/S junction. This was achieved through spin-mixing and spin-rotation from fictitious magnetic fields generated by a nonzero Berry phase. Although topological long-range supercurrents have been demonstrated experimentally, a detailed theory behind spin-triplet superconductivity remains poorly understood. It remains unclear whether long-range supercurrents may be observed at topologically trivial AF Josephson junctions with zero Berry curvature. In particular, equal-spin AR, which is responsible for the conversion of spin-singlet to spin-triplet pairings at the AF/S interface, remains underexplored.

Inspired by previous work, we theoretically study the AR-induced conductance in AF/AF/S junctions with hexagonal lattices. Simultaneous time reversal and spatial inversion, known as parity-time (PT) symmetry, is broken in the AF [39,42,58] when the staggered sublattice potential is introduced. The AF becomes spin splitting in this case [39,58,59]. Spin-flip scattering occurs when the Néel vectors of the AFs are noncollinear, leading to equal-spin AR. We first analyze the effect of the staggered sublattice potential and the electrostatic potential on the AR-induced conductance spectra, and we discover that the conductance spectra can be used to confirm the equal-spin AR signature. Further evidence for the existence of equal-spin AR can then be obtained by investigating the conversion of spin-singlet to spin-triplet pairing correlations. Pairing correlations with spin-down quasiparticles decrease rapidly when the left AF is fully spin-polarized. Meanwhile, the long-range equal-spin triplet pairing correlation $f_{\uparrow\uparrow}$ leads to the conversion from spin-singlet to spin-triplet pairing in the left AF. The study focuses on the magnetoanisotropic conductance induced by conventional and equal-spin ARs. The magnetoanisotropy of the conductance is relatively weak due to the competing contributions of conventional and equal-spin ARs. However, significant anisotropic magnetoresistance is shown when only equal-spin

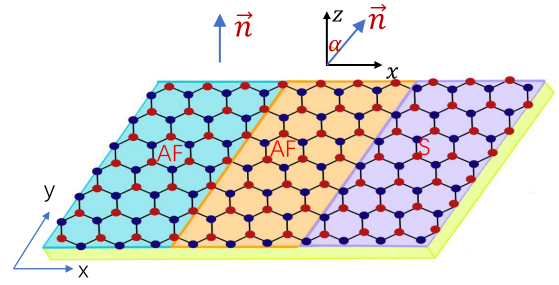


FIG. 1. The schematic diagram for the AF/AF/S junction with the Néel vector \vec{n} along the z ($\vec{n} = (\sin\alpha, 0, \cos\alpha)$) direction for the left (central) AF.

AR is present. It should be noted that while Ref. [46] studied the impact of Rashba spin-orbit coupling and the interaction between the staggered sublattice potential and the antiferromagnetic field on conductance spectra in AF/normal/S junctions, it differs significantly from our work and does not affect novel physics and understanding in our study. Our findings contrast with those of Ref. [46] for several reasons: (i) The equal-spin AR in Ref. [46] and our present work stems from distinct spin-flipping scattering mechanisms. We investigate spin-flipping scattering arising from the noncollinear Néel vectors between the AFs, whereas Ref. [46] considers spin-flipping scattering from Rashba spin-orbit coupling. While Ref. [46] observes a transition from a conductance peak to conductance peak splitting around $E = \Delta_0$, this phenomenon is not present in our results. (ii) Our main focus is on the anisotropic AR, which can serve as a distinctive signature of equal-spin AR, but this is not covered in Ref. [46]. (iii) The pairing correlations are studied in our work, providing further evidence for the existence of equal-spin AR. This aspect is not covered in Ref. [46].

The rest of the paper is organized as follows. Section II describes the system Hamiltonian and the low-energy band structures before establishing the conductance formula through the AR and quasiparticle transmission coefficients, as well as spin-singlet and spin-triplet pairing correlations. Section III focuses on the AR-induced conductance and how the electrostatic potential and the staggered sublattice affect it. The effect of the electrostatic potential and the orientation of the Néel vector of the central AF on the spin-singlet and spin-triplet pairing correlations in the AFs is then discussed. Finally, the magnetoanisotropy of the conductance induced by equal-spin and conventional ARs is addressed. Section IV is a summary of our key findings.

II. MODEL AND FORMULATION

Figure 1 shows a two-dimensional AF/AF/S junction formed by sandwiching an AF layer between an AF and S with hexagonal lattices along the x direction. The AF order in hexagonal lattices would be naturally realized in transition-metal oxides [60] or caused by the substrate [39,58,59]. The AF is typically a spin degeneracy protected by the PT symmetry. If the PT symmetry is broken by introducing the staggered sublattice potential, the AF can become spin splitting [39,42,58,59]. The Néel vector of the left AF is

considered to be along the z axis, whereas that of the central AF lies within the x - z plane at an angle of α to the z axis. In the S, the superconductivity is induced by attaching an s -wave S to the hexagonal lattices [39,42–44]. The tight-binding Hamiltonian of the junction can be expressed as

$$H = -t \sum_{(ij)\sigma} c_{i\sigma}^{\dagger} c_{j\sigma} + \sum_{j\sigma\sigma'} \xi_j [\Delta\sigma_0 - \Delta_{AF}(\vec{\sigma} \cdot \vec{n})]_{\sigma\sigma'} c_{j\sigma}^{\dagger} c_{j\sigma'} - \sum_{j\sigma} U_{j_x} c_{j\sigma}^{\dagger} c_{j\sigma} + \sum_{j\sigma} (\sigma \Delta_0 c_{j\sigma}^{\dagger} c_{j-\sigma}^{\dagger} + \sigma \Delta_0^{\dagger} c_{j-\sigma} c_{j\sigma}). \quad (1)$$

Here, $c_{j\sigma}^{\dagger}$ ($c_{j\sigma}$) represents the creation (annihilation) operator of an electron with spin- σ at site $j = (j_x, j_y)$, and σ_0 is the unit matrix. The first term accounts for nearest-neighbor hopping

$$H = -t \sum_{j_x k_y \sigma} [c_{j_x k_y \sigma}^{A+} c_{j_x+1 k_y \sigma}^B e^{-\frac{i}{2} k_y a} + c_{j_x k_y \sigma}^{A+} c_{j_x-1 k_y \sigma}^B e^{-\frac{i}{2} k_y a} + c_{j_x k_y \sigma}^{A+} c_{j_x k_y \sigma}^B e^{i k_y a} + \text{c.c.}] + \sum_{j_x k_y \sigma \sigma'} [\Delta\sigma_0 - \Delta_{AF}(\vec{\sigma} \cdot \vec{n})]_{\sigma\sigma'} [c_{j_x k_y \sigma}^{A+} c_{j_x k_y \sigma'}^A - c_{j_x k_y \sigma}^{B+} c_{j_x k_y \sigma'}^B] - \sum_{j_x k_y \sigma} U_{j_x} [c_{j_x k_y \sigma}^{A+} c_{j_x k_y \sigma}^A + c_{j_x k_y \sigma}^{B+} c_{j_x k_y \sigma}^B] + \sum_{j_x k_y} \Delta_0 [c_{j_x k_y \uparrow}^{A+} c_{j_x-k_y \downarrow}^{A+} + c_{j_x k_y \uparrow}^{B+} c_{j_x-k_y \downarrow}^{B+} + \text{c.c.}]. \quad (2)$$

The low-energy band structures can provide clear insights into the properties of the AR processes, which are responsible for the subgap conductance. The Hamiltonian in momentum space can be obtained by performing a Fourier transform on the Hamiltonian (1). The low-energy Hamiltonian of the AF is given by [8,42,60]

$$H = \hbar v_F (\eta k_x \tau_x + k_y \tau_y) + (\Delta - \sigma \Delta_{AF}) \tau_z - U_{j_x}. \quad (3)$$

Here, $\eta = +(-)$ corresponds to the K (K') valley, and $\tau = (\tau_x, \tau_y, \tau_z)$ is the Pauli matrix denoting the sublattice pseudospin. $v_F = 3at/2\hbar$ is the Fermi velocity, and k_x and k_y are the wave vectors in the x and y directions. The band structure for the spin- σ electrons can be described as

$$E = \pm \sqrt{(\hbar v_F)^2 (k_x^2 + k_y^2) + (\Delta - \sigma \Delta_{AF})^2} - U_{j_x}, \quad (4)$$

where $+$ and $-$ refer to the conduction and valence bands. When both Δ and Δ_{AF} are finite simultaneously, the spin degeneracy in the AF is removed.

Consider an electron with energy E incident from the AF. The conductance calculated by the nonequilibrium Green's function method is expressed as [8,46,61,62]

$$G = \frac{e^2}{h} (2T_A + T_Q), \quad (5)$$

where T_A represents the AR coefficient, and $T_Q = \frac{1}{W} \sum_{k_y} \text{Tr}[\Gamma_{Le}^{\dagger} (G^{\dagger} \Gamma_R G^a)_{ee}]$ is the quasiparticle transmission coefficient. $k_y = 2\pi n/W$ is the transverse momentum, with W representing the transverse width of the junction and n being an integer to denote the channels. $G^{r(a)}$ is the retarded (advanced) Green's function of the central

with a hopping energy t . Δ corresponds to the staggered sublattice potential, where $\xi_j = +(-)$ indicates the A (B) site, which can be intrinsic [60] or induced by the substrate [39,42,58]. Δ is denoted as $\Delta_{L(C)}$ for the left (central) AF. The third term describes the collinear antiferromagnetic exchange field with strength Δ_{AF} . In the left AF, the Néel vector is aligned with the z axis; in the central AF, it is aligned with the $\vec{n} = (\sin\alpha, 0, \cos\alpha)$. U_{j_x} represents the electrostatic potential, with $U_{j_x} = U$ for the left AF ($j_x \leq N$), $U_{j_x} = eV_g$ ($N < j_x \leq N + N_x$) for the central AF, and $U_{j_x} = \mu_s$ for the S ($j_x > N + N_x$). The last term denotes the superconducting pairing term with the superconducting gap Δ_0 . $L = N_x \sqrt{3}a/2$, with a as the lattice constant, representing the length of the central AF. Along the y direction, the translational symmetry is conserved, allowing the electron momentum k_y to serve as a good quantum number. Consequently, summation over j_y sites in Eq. (1) can be transformed into momentum space,

AF, with the linewidth function for the left (right) lead denoted as $\Gamma_{L(R)}$ (for more details, refer to Appendix A). In the presence of spin-flip scattering, T_A can be written as $T_A = \sum_{\sigma} (T_{AR\sigma\bar{\sigma}} + T_{AR\sigma\sigma})$, where $T_{AR\sigma\bar{\sigma}}$ and $T_{AR\sigma\sigma}$ are the conventional and equal-spin AR coefficients, respectively. The conventional AR coefficient can be expressed as [8,46,61]

$$T_{AR\sigma\bar{\sigma}} = \frac{1}{W} \sum_{k_y} \text{Tr}(\Gamma_{Le}^{\sigma} G_{eh\sigma\bar{\sigma}}^r \Gamma_{Lh}^{\bar{\sigma}} G_{he\sigma\bar{\sigma}}^a), \quad (6)$$

where the electron and hole come from different spin bands, leading to a spin-singlet pairing with opposite spins. Here $\bar{\sigma}$ is opposite to σ with $\sigma = \uparrow, \downarrow$. e (h) labels the electron (hole) component of the Nambu space. $\Gamma_{Le}^{\uparrow(\downarrow)}$ or $\Gamma_{Lh}^{\uparrow(\downarrow)}$ are the spin-up (spin-down) electron or hole block of the linewidth function Γ_L , while the equal-spin AR coefficient is written as [8,46,61]

$$T_{AR\sigma\sigma} = \frac{1}{W} \sum_{k_y} \text{Tr}(\Gamma_{Le}^{\sigma} G_{eh\sigma\sigma}^r \Gamma_{Lh}^{\sigma} G_{he\sigma\sigma}^a), \quad (7)$$

where the incident electron and Andreev-reflected hole come from the same spin band, forming a spin-triplet pairing with parallel spins. Here, we compare the conductance formula with the one derived from the Blonder-Tinkham-Klapwijk approach as presented in Ref. [63]. For $E < \Delta_0$, T_Q is zero and we have the relationship $1 - \frac{k_{\uparrow 1}^{\dagger}}{k_{\uparrow 1}} |b_{s\uparrow}|^2 - \frac{k_{\downarrow 1}^{\dagger}}{k_{\downarrow 1}} |b_{s\downarrow}|^2 = \frac{k_{\uparrow 1}^{\dagger}}{k_{\uparrow 1}} |a_{s\uparrow}|^2 + \frac{k_{\downarrow 1}^{\dagger}}{k_{\downarrow 1}} |a_{s\downarrow}|^2$ [63]. This relation allows us to calculate the conductance as $G = \sum_s 2(\frac{k_{\uparrow 1}^{\dagger}}{k_{\uparrow 1}} |a_{s\uparrow}|^2 + \frac{k_{\downarrow 1}^{\dagger}}{k_{\downarrow 1}} |a_{s\downarrow}|^2) = 2T_A$. Considering a spin-up electron incident from the left AF, we

observe the relation $T_{AR\uparrow\uparrow} = \frac{k_{\uparrow 1}^-}{k_{\uparrow 1}^+} |a_{\uparrow\uparrow}|^2$ and $T_{AR\uparrow\downarrow} = \frac{k_{\uparrow 1}^-}{k_{\uparrow 1}^+} |a_{\uparrow\downarrow}|^2$.

However, for $E > \Delta_0$, the equation changes to $1 - \frac{k_{\uparrow 1}^+}{k_{\uparrow 1}^-} |b_{s\uparrow}|^2 - \frac{k_{\downarrow 1}^+}{k_{\downarrow 1}^-} |b_{s\downarrow}|^2 \neq \frac{k_{\uparrow 1}^-}{k_{s1}^+} |a_{s\uparrow}|^2 + \frac{k_{\downarrow 1}^-}{k_{s1}^+} |a_{s\downarrow}|^2$, indicating that electrons or holes can tunnel into the S, and T_Q becomes finite.

To gain a better insight into conventional and equal-spin ARs, we study the spin-singlet and spin-triplet pairing correlations in the AF regions. This helps us to understand the conversion from spin-singlet to spin-triplet pairings. We calculate the retarded Green's function at site j_x in the Nambu basis,

$$G^r(j_x, j_x, k_y, \omega) = \begin{pmatrix} G_{ee}^r & G_{eh}^r \\ G_{he}^r & G_{hh}^r \end{pmatrix}, \quad (8)$$

where G_{ee}^r and G_{eh}^r correspond to the normal and anomalous components. In this case, we have the pair amplitudes $f = \frac{1}{W} \sum_{k_y} G_{eh}^r(j_x, j_x, k_y)$. The spin-singlet and mixed spin-triplet pairing correlations ($\uparrow\downarrow \mp \downarrow\uparrow$) with spin-projection $S_z = 0$ are represented by f_0 and f_3 , respectively, whereas the spin-polarized triplet pairing correlations ($\uparrow\uparrow$ and $\downarrow\downarrow$) with spin-projection $S_z = 1$ are denoted by $f_{\uparrow\downarrow}$ and $f_{\downarrow\downarrow}$ (Appendix B) [64–67]. According to Fermi-Dirac statistics, f_0 is even in frequency, while the other pairing correlations are odd in frequency [65]. Since the pairing correlation f_β ($\beta = 0, 3, \uparrow\uparrow$, and $\downarrow\downarrow$) is often a complex number, we will focus throughout this paper on the amplitude of f_β , which is defined as $|f_\beta| = \sqrt{f_\beta f_\beta^*}$ [65].

III. RESULTS AND DISCUSSIONS

A. Conventional and equal-spin ARs

We first study the band structures of the left AF described by Eq. (4), as they can provide clear insights into the AR processes. The AF is typically spin degeneracy protected by the PT symmetry. Introducing the staggered sublattice potential Δ_L can break this symmetry. In this case, the energy gap in one spin band decreases, while the energy gap in the opposite spin band increases. The band of the AF is split into spin-up and spin-down bands, with a spin-dependent energy gap of $E_{g\sigma} = 2|\lambda_v - \sigma\lambda_{AF}|$. $|E + U| > E_{g\sigma}/2$ should be satisfied to generate propagating incident modes in the spin- σ channel. The spin polarization of the AF increases as U decreases, reaching 100% spin polarization at low U , when only one spin band is active. Thus, adjusting Δ_L and U enables the manipulation of the AF's spin polarization. Similarly, spin polarization can be realized in the central AF due to the interplay of the staggered sublattice potential and the antiferromagnetic exchange field. We assume that both the spin-up and spin-down bands are active in the central AF, enabling the coexistence of spin-singlet and spin-triplet pairing correlations in this region. Consider an incoming electron with incident energy E from the left AF. If $|E + U| < |\Delta_L - \Delta_{AF}|$ is satisfied, the incident energy resides in the energy gaps of the spin-up and spin-down electrons. This means that there are no propagating incident modes in the left AF, hence the conductance is zero. Tuning U or Δ_L can lead to $|\Delta_L - \Delta_{AF}| < E + U < \Delta_L + \Delta_{AF}$, in which incident energy only

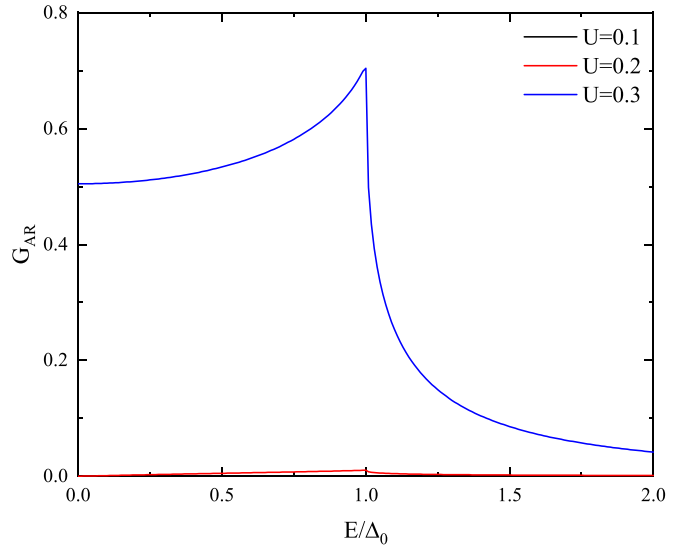


FIG. 2. G_{AR} vs E at different U with the Néel vectors of the AFs collinear. The parameters are $\Delta_L = \Delta_{AF} = 0.1$, $\Delta_c = 0.2$, $eV_g = 0.5$, $\mu_s = 0.2$, and $N_x = 10$.

crosses the spin-up band, resulting in 100% spin polarization. In this case, the AR processes involving spin-down quasiparticles are excluded, so the conventional AR is not allowed. Spin-flip scattering occurs when the Néel vectors of the AFs are noncollinear. An equal-spin AR appears when an incoming spin-up electron is reflected into a spin-up hole. When $E + U > |\Delta_L + \Delta_{AF}|$ is satisfied, the incident energy crosses the conduction bands of the spin-up and spin-down quasiparticles, allowing both conventional and equal-spin ARs to occur simultaneously. The above discussion suggests that U and Δ_L play a significant role in the spin polarization of the left F; consequently, these parameters can be tuned to control the magnitude of both conventional and equal-spin ARs.

Figure 2 shows the conventional AR-induced conductance $G_{AR} = \frac{2e^2}{h}(T_{AR\uparrow\downarrow} + T_{AR\downarrow\uparrow})$, which occurs when an incoming spin- σ electron reflects into the hole with the opposite spin. We have scaled U , eV_g , Δ_L , Δ_c , and Δ_{AF} in units of t with $t = 1$. The superconducting gap Δ_0 is fixed at 0.001. The band structures of the central AF are spin-polarized due to the interaction between Δ_c and Δ_{AF} . In this work, the incident energy lies in the spin-up and spin-down conduction bands of the central AF. We assume that the Néel vectors of the AFs are collinear ($\alpha = 0$), so that spin-flip scattering is absent and only conventional AR is possible. For the parameters used here, the spin-down band exhibits an energy gap, while the spin-up band is gapless. The incident energy is only in the spin-up band of the left AF for $|E + U| < 0.2$. At $U = 0.1$, G_{AR} is zero because the conventional AR disappears due to the lack of spin-down quasiparticles. Subsequently, at $U = 0.2$, the incident energy is located at the bottom of the spin-down conduction band of the left AF. Although an incident spin-down electron can be reflected into a spin-up hole in the left AF, the low density of states results in vanishing G_{AR} . Conversely, at $U = 0.3$, both spin-up and spin-down quasiparticles are present, leading to a large G_{AR} .

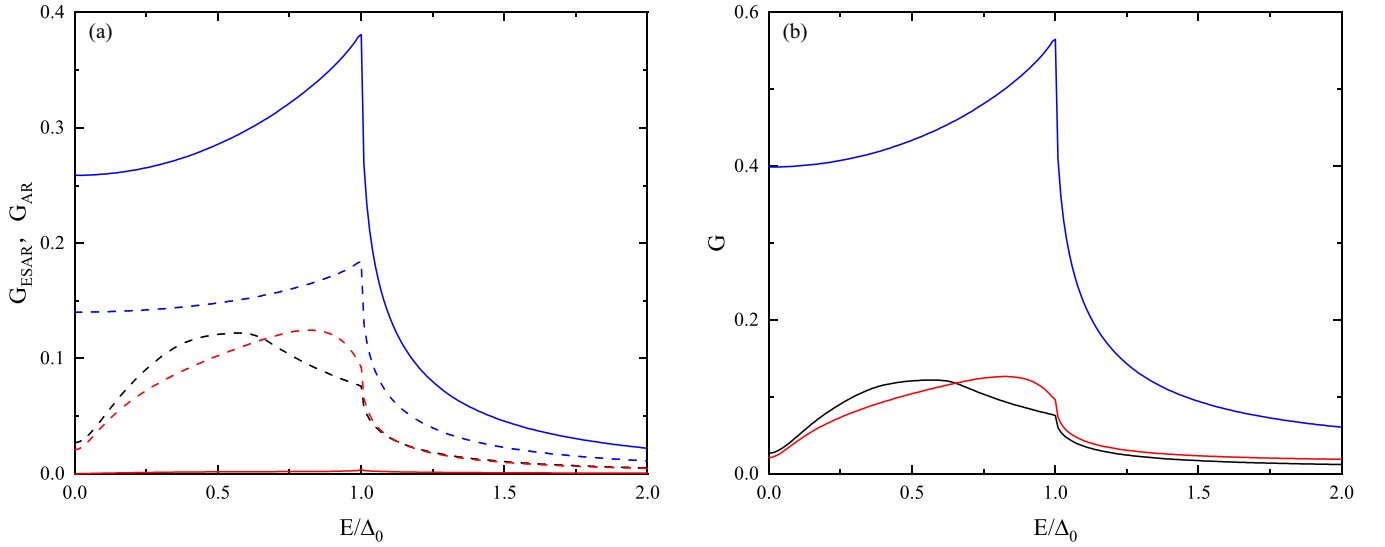


FIG. 3. (a) G_{AR} (solid) and G_{ESAR} (dashed); (b) G vs E at different U , with the Néel vectors of the AFs noncollinear ($\alpha = \pi/2$). The black, red, and blue lines correspond to $U = 0.1, 0.2, 0.3$, respectively. Other parameters are the same as in Fig. 2.

Since our focus is on the equal-spin Andreev reflection, which occurs when the Néel vectors of the left and central AFs are noncollinear, we set $\alpha = \pi/2$. In Fig. 3(a), we plot G_{AR} and the equal-spin AR-induced conductance $G_{\text{ESAR}} = \frac{2e^2}{h}(T_{\text{AR}\uparrow\uparrow} + T_{\text{AR}\downarrow\downarrow})$ as functions of E at different U . In addition to conventional AR, spin-flip scattering also generates equal-spin AR. Similar to Fig. 2, at $U = 0.1$ and 0.2 , G_{AR} tends to zero because there are no spin-down incident quasiparticles. For high U , both spin-up and spin-down quasiparticles are present in the left AF, leading to a large G_{AR} . Unlike G_{AR} , the spin-up linear band structure ensures that G_{ESAR} is always finite. G_{ESAR} shows different behavior for $U = 0.1, 0.2$ compared to $U = 0.3$. For $U = 0.3$, G_{ESAR} increases with E and peaks at $E = \Delta_0$, comparable to G_{AR} . However, G_{ESAR} dips at $E = 0$, increases with E , and peaks

at the subgap energy rather than $E = \Delta_0$. Figure 3(b) shows the conductance spectra at different U . For $U = 0.1$ and 0.2 , G is determined by G_{ESAR} . In these cases, G increases with E , reaches a peak at some E within the superconducting gap rather than $E = \Delta_0$, and then begins to decrease. At $U = 0.3$, G comes from both G_{AR} and G_{ESAR} and is determined by G_{AR} , in contrast to $U = 0.1, 0.2$. G increases with E and reaches its maximum at $E = \Delta_0$. Since the conductance spectra of the conventional and equal-spin ARs are different, the signature of the equal-spin AR can be confirmed by studying the conductance spectra.

We study how Δ_L affects G_{AR} and G_{ESAR} at $U = 0.3$ and $\alpha = \pi/2$ in Fig. 4(a). For $\Delta_L = 0.1$, the spin-down band structures have an energy gap of 0.2 , but the spin-up ones have the linear dispersion relation with no energy gap. In this case,

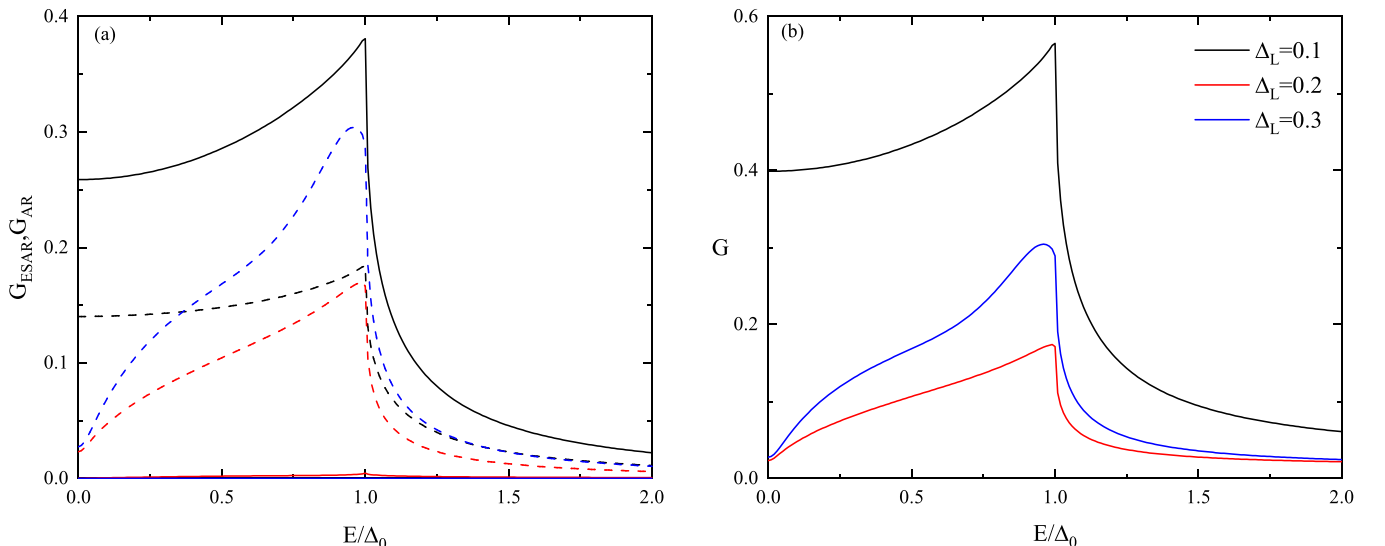


FIG. 4. (a) G_{AR} (solid) and G_{ESAR} (dashed), and (b) G vs E at different Δ_L , with $\alpha = \pi/2$. The black, red, and blue lines correspond to $\Delta_L = 0.1, 0.2, 0.3$, respectively. Other parameters are the same as in Fig. 2.

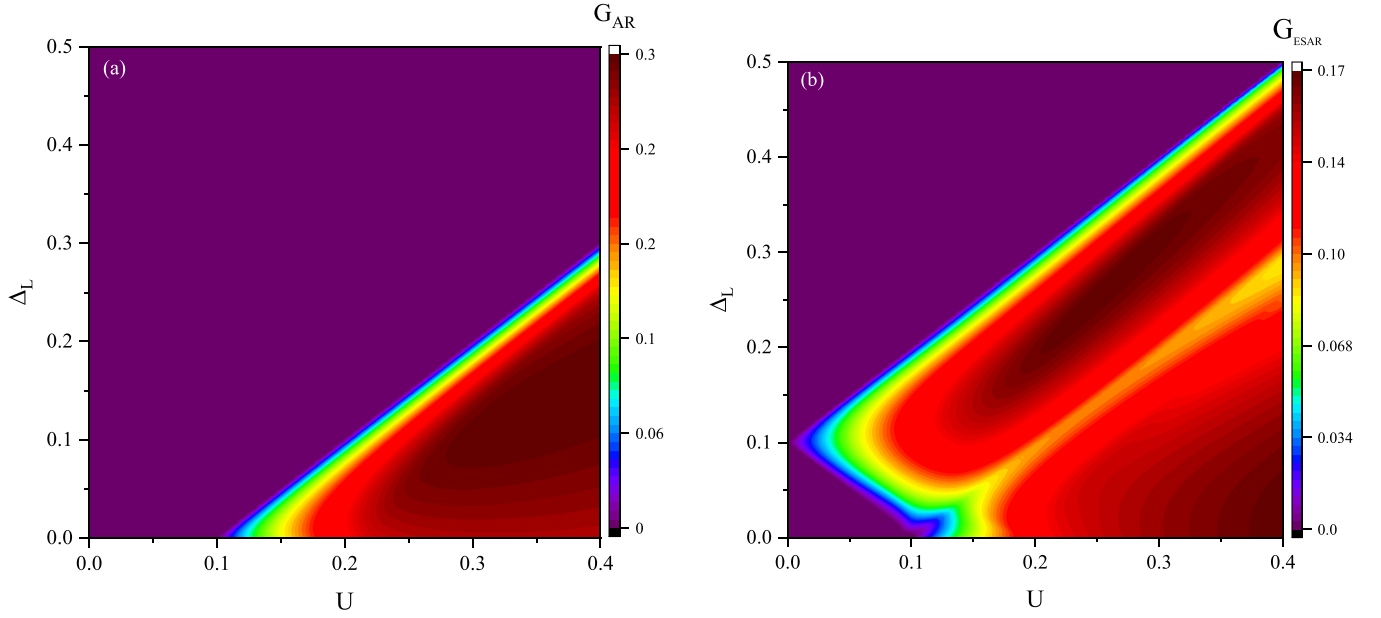


FIG. 5. Panels (a) and (b) depict G_{AR} and G_{ESAR} as functions of U and Δ_L . Here, we set $E/\Delta_0 = 0.5$ and $\alpha = \pi/2$, and other parameters are the same as in Fig. 2.

both spin-up and spin-down states are present, and thus a high G_{AR} is observed. When $\Delta_L = 0.2$, the spin-down (spin-up) quasiparticles have an energy gap of 0.3 (0.1). The incident energy is positioned at the bottom of the spin-down conduction band of the left AF. Given the low density of states, G_{AR} approaches 0, while for $\Delta_L = 0.3$ the spin-down (spin-up) quasiparticles have an energy gap of 0.4 (0.2). Since the incident energy resides in the energy gap of spin-down quasiparticles, conventional AR is forbidden due to the absence of spin-down states. In contrast to G_{AR} , G_{ESAR} remains finite since the incident energy falls within the spin-up conduction band. When both spin-up and spin-down states are present, both G_{AR} and G_{ESAR} exhibit similar behaviors. Conversely, when only spin-up quasiparticles are available, G_{AR} becomes zero while G_{ESAR} shows distinct behavior [as depicted by the blue lines in Fig. 4(a)]. Figure 4(b) displays the conductance spectra at different Δ_L . For $\Delta_L = 0.1$, G is determined by G_{AR} , which increases with E and reaches a peak at $E = \Delta_0$, while for large Δ_L , G only originates from G_{ESAR} , which has a dip at $E = 0$, increases with E , and then reaches a peak near $E = \Delta_0$.

To further understand the influence of U and Δ_L on the AR-induced conductance, a 2D plot of G_{AR} and G_{ESAR} as functions of U and Δ_L is investigated in Fig. 5. In Fig. 5(a), it is observed that G_{AR} is always zero in the region of $E + U < \Delta_L + \Delta_{AF}$. This can be attributed to the absence of spin-down quasiparticles, given that the incident energy resides within the energy gap of the spin-down band. For high U or small Δ_L , the incident energy falls within the conduction bands of both spin-up and spin-down quasiparticles, hence G_{AR} becomes finite. For a fixed Δ_L , G_{AR} increases with U as the density of states increases. In Fig. 5(b), three distinct transport regions are identified based on the behavior of G_{ESAR} . In the first region where $E + U < |\Delta_L - \Delta_{AF}|$, the incident energy is in the energy gaps of the spin-up and spin-down quasiparticles, and thus no AR is allowed, resulting in zero

G_{ESAR} and G_{AR} [Figs. 5(a) and 5(b)]. In the second region, defined by $|\Delta_L - \Delta_{AF}| < E + U < \Delta_L + \Delta_{AF}$, the incident energy is in the conduction band of the spin-up quasiparticles and the energy gap of the spin-down ones, therefore G_{ESAR} is finite with zero G_{AR} . Finally, in the region where $E + U > |\Delta_L + \Delta_{AF}|$, the incident energy lies in the conduction bands of spin-up and spin-down quasiparticles, therefore G_{ESAR} is always finite with nonzero G_{AR} . Thus, by adjusting U and Δ_L , we can control the amplitudes of G_{AR} and G_{ESAR} to obtain pure equal-spin AR.

B. Spin-singlet and spin-triplet pairing correlations

Next, we explore how spin-singlet and spin-triplet pairing correlations evolve in the AF regions. The amplitude of the AR is linked to the proximity-induced pairing correlations, as described by the anomalous Green's function. Conventional AR can create superconducting singlet correlations, while equal-spin AR induces spin-polarized triplet correlations. As previously stated, by adjusting Δ_L and U , the spin polarization of the AF can be modified, leading to a substantial impact on the amplitude of the AR, so the pairing correlations in the AF regions are expected to be influenced by both Δ_L and U . We consider two conditions: (i) $|\Delta_L - \Delta_{AF}| < E + U < \Delta_L + \Delta_{AF}$, and (ii) $E + U > \Delta_L + \Delta_{AF}$. Tuning U or Δ_L to satisfy the first condition, which involves only the spin-up band and results in 100% spin polarization, the pairing correlation amplitudes, including those of spin-down quasiparticles, rapidly decay to zero as the position within the left AF deviates from the AFs' interface. Spin-flip scattering occurs when the Néel vectors of the AFs are noncollinear, causing the conversion from spin-singlet to spin-triplet pairings. $f_{\uparrow\uparrow}$ is immune to strong spin polarization and can penetrate deeper into the left AF region. When the second condition of $E + U > |\Delta_L + \Delta_{AF}|$ is satisfied, spin-up and spin-down conduction bands become active. This allows the conversion of spin-singlet

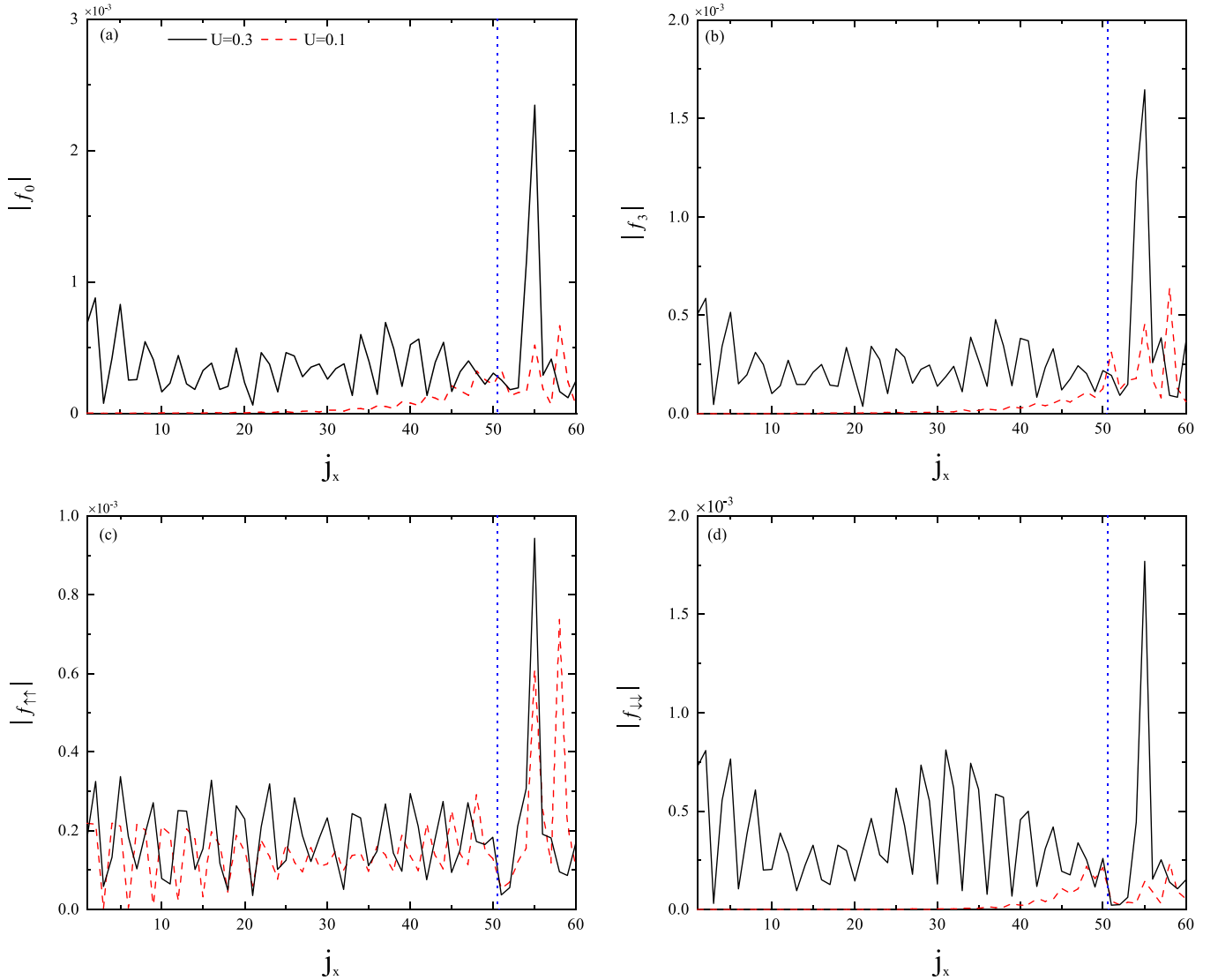


FIG. 6. (a) $|f_0|$, (b) $|f_3|$, (c) $|f_{\uparrow\uparrow}|$, and (d) $|f_{\downarrow\downarrow}|$ at $U = 0.3$ (black) and $U = 0.1$ (red) as a function of j_x in the AFs. The dotted line represents the interface between the left and central AFs. Other parameters are the same as in Fig. 5.

pairings into spin-triplet pairings, allowing them to coexist. We then investigate how varying U affects the spin-singlet and spin-triplet pairings. It is worth noting that the effect of Δ_L on these pairing correlations shows a similar behavior (not shown here).

Figure 6 demonstrates how the pairing correlations vary with the position j_x in the central AF ($50 < j_x \leq 60$) and the left AF ($j_x \leq 50$). The central region's Δ_c and eV_g are set to $\Delta_c = 0.2$ and $eV_g = 0.5$, respectively. This suggests that both the spin-up and spin-down conduction bands are active in the central AF. The Néel vectors of the AFs are perpendicular, and thus the spin-triplet pairing correlations in the AF near the AF/S interface can be generated by spin-flip scattering. The absolute value of $|f_\beta|$ ($\beta = 0, 3, \uparrow\uparrow, \downarrow\downarrow$) is always finite and exhibits spatial oscillations within the central AF. At $U = 0.3$, both the spin-up and spin-down conduction bands are active in the left AF, resulting in a finite and spatially oscillating $|f_\beta|$. This corresponds to the existence of both conventional and equal-spin ARs, as shown in Figs. 3 and 4. For $U = 0.1$, the pairing correlations f_0 , f_3 , and $f_{\downarrow\downarrow}$ decrease rapidly when

j_x deviates from the interface between the AFs, which can be attributed to the absence of the spin-down quasiparticles. However, the equal-spin triplet pairing correlation $f_{\uparrow\uparrow}$ exhibits long-range behavior, therefore only equal-spin triplet pairing is seen when the position in the left AF is far from the interface between the AFs. This observation is consistent with Figs. 3 and 4, where only equal-spin AR is observed at $U = 0.1$.

Figure 7 shows how α affects the spin-singlet and spin-triplet pairing correlations in the AFs. In the central AF where both spin-up and spin-down bands are present, any pairing correlation can exist. We focus on the conversion from spin-singlet to spin-triplet pairing correlations, so for the parameters used here, only the spin-up band is active in the left AF. Due to the absence of spin-flip scattering, equal-spin spin-triplet pairing correlations ($\uparrow\uparrow$ and $\downarrow\downarrow$) do not exist in the AFs when the Néel vectors of the AFs are collinear ($\alpha = 0$). The amplitudes of f_0 and f_3 decrease rapidly as j_x moves away from the interface between the AFs due to the lack of spin-down quasiparticles in the left AF. Spin-flip scattering

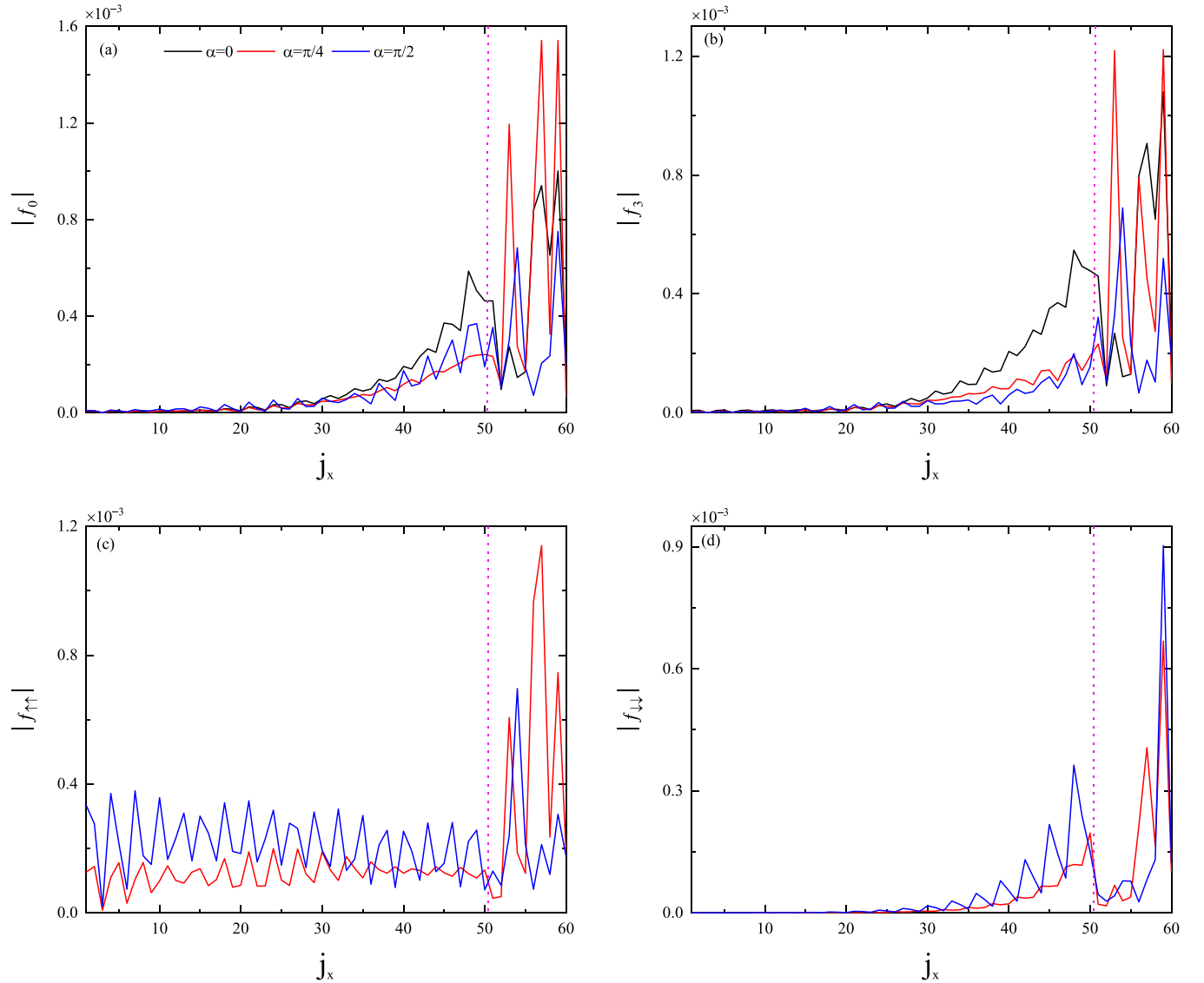


FIG. 7. (a) $|f_0|$, (b) $|f_3|$, (c) $|f_{\uparrow\uparrow}|$, and (d) $|f_{\downarrow\downarrow}|$ at $\alpha = 0$ (black), $\alpha = \pi/4$ (red), and $\alpha = \pi/2$ (blue) as a function of j_x in the AFs. The dotted line represents the interface between the left and central AFs. We set $U = 0.15$, and other parameters are the same as in Fig. 5.

happens when the Néel vectors of the AFs are noncollinear ($\alpha \neq 0$). Spin-singlet pairing correlations decay rapidly with j_x and can be transformed into spin-triplet pairing correlations. f_0 , f_3 , and $f_{\downarrow\downarrow}$, which involve spin-down quasiparticles, show similar trends, represented by the red and blue lines in Fig. 7. Conversely, $f_{\uparrow\uparrow}$ arises solely from spin-up quasiparticles, exhibits spatial oscillations, and enables long-range correlations within the left AF. As α increases, the amplitude of $f_{\uparrow\uparrow}$ increases, as shown in Fig. 7(c). The long-range supercurrent in the AF/S Josephson junction depends strongly on $f_{\uparrow\uparrow}$. Indeed, long-range Josephson currents through a chiral noncollinear AF in the Josephson junction have been experimentally observed [41].

C. Conventional and equal-spin AR-induced magnetoanisotropic conductance

While the signature of the presence of equal-spin AR can be confirmed by studying the conductance spectra and

pairing correlations, the magnetoanisotropic transport properties provide another clear indicator. As previously stated, when $\alpha = 0$, only conventional AR and proximity-generated spin-singlet pairing correlation f_0 and the mixed spin-triplet correlation f_3 are present. When $\alpha = \pi/2$, equal-spin AR and spin-polarized triplet pairing correlations $f_{\uparrow\uparrow}$ and $f_{\downarrow\downarrow}$ are also seen. In this section, we study the magnetoanisotropy of the conventional and equal-spin AR-induced conductance. Figure 8(a) shows a 2D plot illustrating the dependence of G_{AR} on U and α at $E = \Delta_0/2$. When $U + E$ is greater than $\Delta_L + \Delta_{AF}$, the incident energy crosses both the spin-up and spin-down bands. The behavior of G_{AR} with respect to α exhibits a nonmonotonic pattern with a π -periodicity in α . G_{AR} shows a remarkable magnetoanisotropy with maxima at $\alpha = 0, \pi$ and minima at $\alpha = \pi/2$ and $3\pi/2$. Meanwhile, G_{AR} is always zero for $U + E < \Delta_L + \Delta_{AF}$ because of the absence of spin-down quasiparticles in the left AF. The effect of U and α on G_{ESAR} is discussed in Fig. 8(b). Similar to G_{AR} , when $U + E$ is greater than $\Delta_L + \Delta_{AF}$, G_{ESAR} is

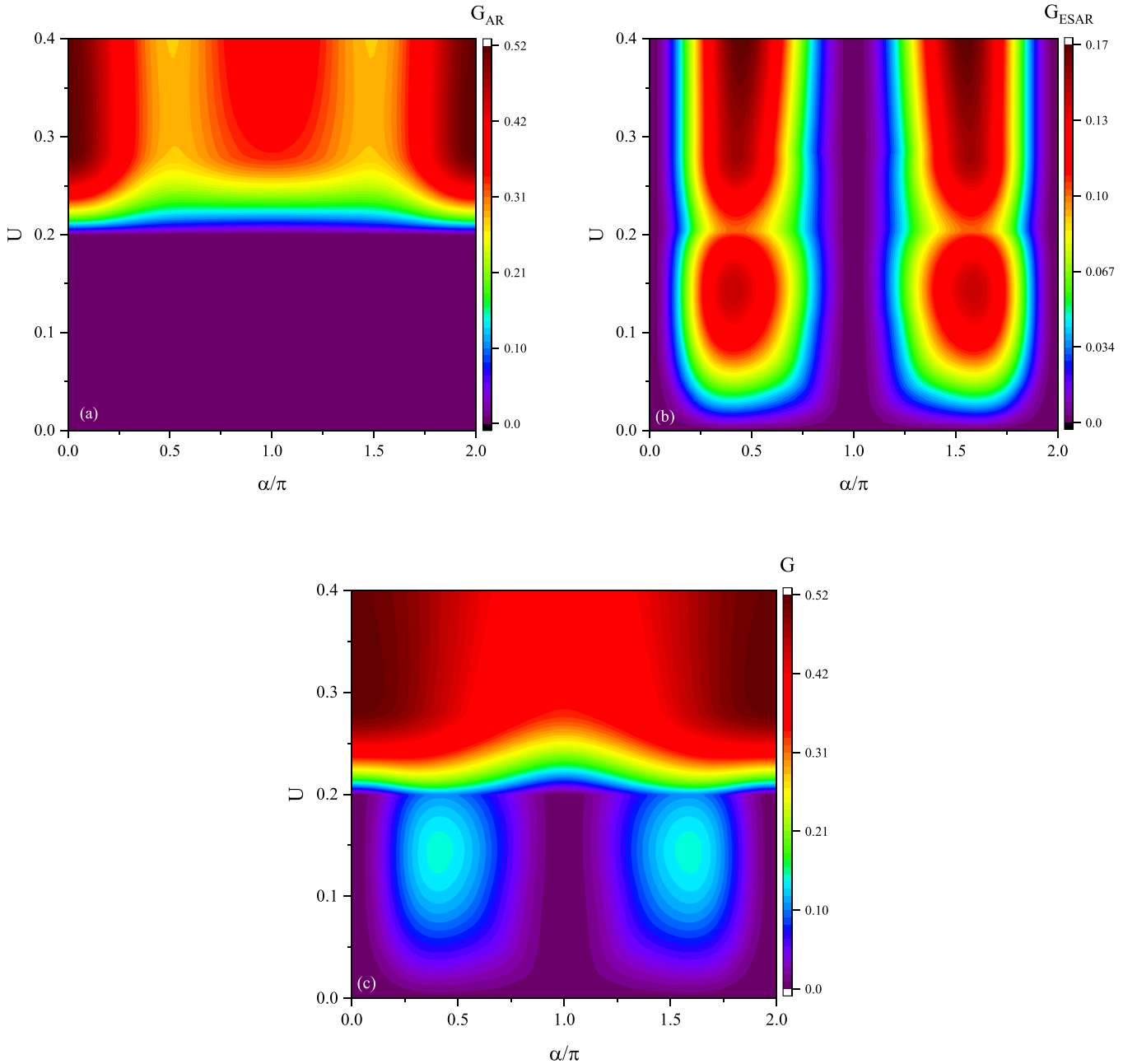


FIG. 8. (a) G_{AR} , (b) G_{ESAR} , and (c) G vs U , and α at $E/\Delta_0 = 0.5$ and $\Delta_L = 0.1$. Other parameters are the same as in Fig. 3.

finite and shows a π -periodic dependence on α . A comparison between Figs. 8(a) and 8(b) reveals that the maxima in G_{AR} correspond to the minima in G_{ESAR} and vice versa. This is because spin-flip scattering can induce the conversion from spin-singlet to spin-triplet pairing correlations. Unlike G_{AR} , G_{ESAR} is nonzero even in the completely spin-polarized region of $U + E < \Delta_L + \Delta_{AF}$. As G_{ESAR} has a π -periodic dependence on α , we specifically analyze its behavior within the range of $0 \leq \alpha \leq \pi$. G_{ESAR} is zero for $\alpha = 0, \pi$ due to the absence of spin-flip scattering. The strength of the spin-flip scattering increases with α and reaches its maximum at $\alpha = \pi/2$ before decreasing, leading to a nonmonotonic dependence of G_{ESAR} on α . Given that actual experiments primarily investigate the total subgap conductance $G = G_{AR} + G_{ESAR}$, rather than focusing solely on G_{AR} and G_{ESAR} , Fig. 8(c)

illustrates how G varies with U and α . For $U + E > \Delta_L + \Delta_{AF}$, the magnetoanisotropy of G is quite weak due to the competing contributions of G_{AR} and G_{ESAR} . Conversely, when $U + E$ is less than $\Delta_L + \Delta_{AF}$, the left AF is fully spin-polarized, and thus G comes only from G_{ESAR} . The anisotropic equal-spin AR leads to a low (high) conductance state at $\alpha = 0$ ($\alpha = \pi/2$) [Fig. 8(c)], consequently resulting in significant anisotropic magnetoresistance. Indeed, Cai *et al.* [12] found highly anisotropic magnetoresistances at F/S junctions and emphasized that this magnetoanisotropy provides experimental support for equal-spin AR and induced spin-triplet superconductivity at the F/S junction.

Since the AR-induced conductance depends strongly on Δ_L and α , a 2D plot of G_{AR} at $E = \Delta_0/2$ as a function of Δ_L and α is shown in Fig. 9(a). For small Δ_L , the condition of

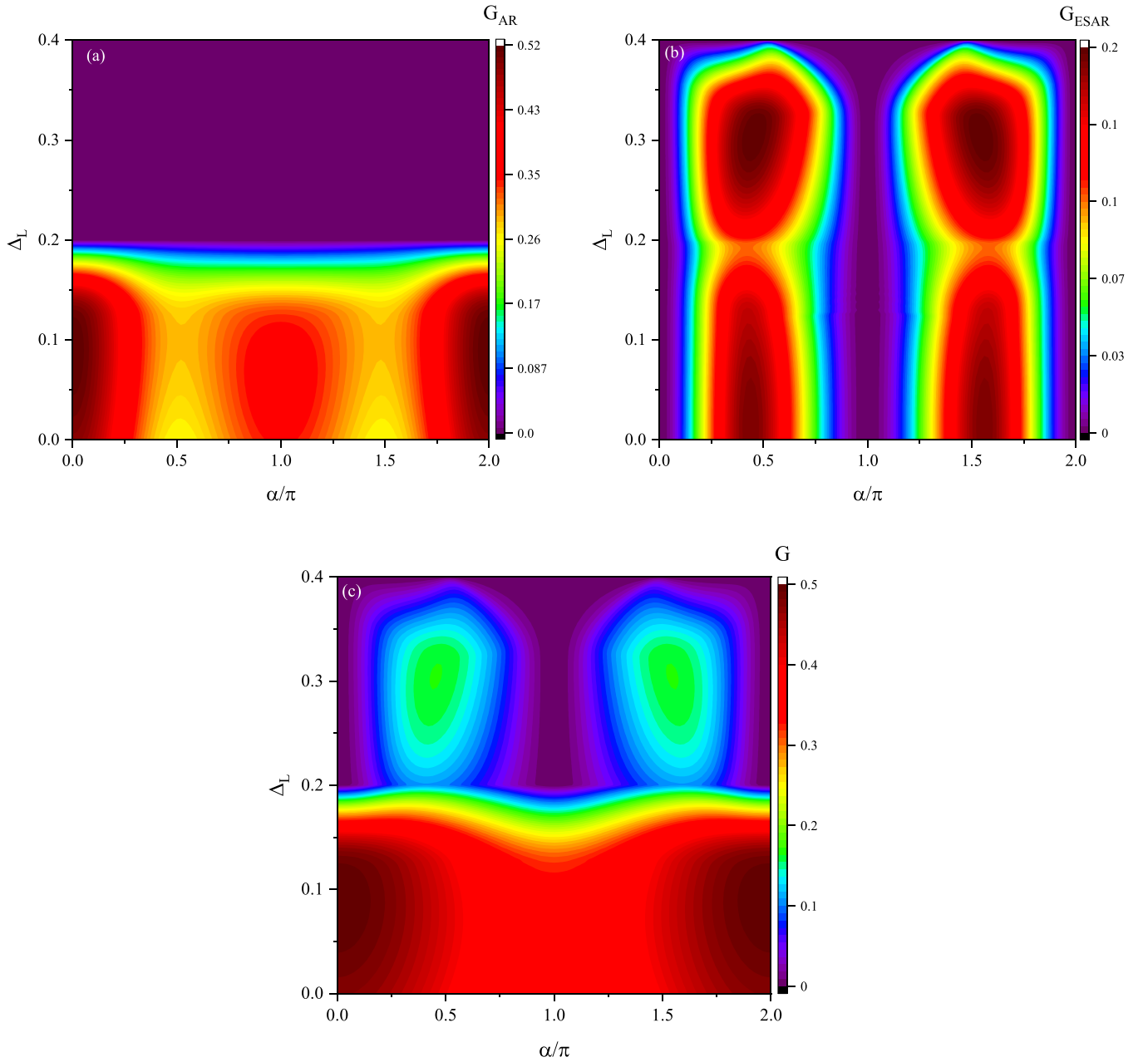


FIG. 9. (a) G_{AR} , (b) G_{ESAR} , and (c) G vs Δ_L , and α at $E/\Delta_0 = 0.5$ and $U = 0.15$. Other parameters are the same as in Fig. 3.

$U + E > \Delta_L + \Delta_{AF}$ is satisfied, thus both spin-up and spin-down conduction bands are involved, resulting in a finite G_{AR} . G_{AR} shows remarkable magnetoanisotropy with a π -periodic dependence on α , with maxima at $\alpha = 0, \pi$ and 2π and minima at $\alpha = \pi/2$ and $3\pi/2$. Conversely, for large Δ_L , G_{AR} becomes zero due to the absence of spin-down quasiparticles. In contrast to G_{AR} , G_{ESAR} is always finite with a π period of α [Fig. 9(b)]. In particular, for $\Delta_L > 0.2$, G_{ESAR} is observed without G_{AR} . Figure 9(c) describes G as a function of Δ_L and α . For $\Delta_L < 0.2$, G_{AR} and G_{ESAR} are finite, and the maxima in G_{AR} correspond to the minima in G_{ESAR} and vice versa. The competition between G_{AR} and G_{ESAR} tends to diminish the magnetoanisotropy of G . Conversely, for large Δ_L , G comes only from G_{ESAR} and shows significant magnetoanisotropy. As a result, equal-spin AR can generate significant anisotropic

magnetoanisotropy at the AF/S interface, providing a signature for the existence of equal-spin AR and spin-triplet pairing in AF/S junctions.

IV. SUMMARY

In summary, we study the AR-induced conductance in AF/AF/S junctions using the nonequilibrium Green's function method. The AF becomes spin-polarized when the PT symmetry is broken. The spin polarization can be controlled by Δ_L and U . Equal-spin AR arises from spin flip scattering when the Néel vectors of the AFs are not collinear. If G is determined by G_{AR} , it increases with E and peaks at $E = \Delta_0$. Conversely, if G comes only from G_{ESAR} , it peaks at E in the superconducting gap, increases with E , and dips at $E = 0$.

Pure equal-spin AR can be obtained by varying U and Δ_L . The different behavior of the conductance spectra for conventional and equal-spin ARs allows the identification of the signature of equal-spin AR. We further investigate how spin-singlet and spin-triplet pairing correlations are formed in the AFs. In a fully spin-polarized left AF, the pairing correlations f_0 , f_3 , and $f_{\downarrow\downarrow}$ decrease rapidly, while $f_{\uparrow\uparrow}$ shows a long-range behavior, so that only equal-spin triplet pairing is seen when the position is deeper in the left AF. Here, we focus on the static limit with zero bias, and our results are consistent with those in Ref. [64], where the inhomogeneous nature of the magnet enables all odd triplet pairing components to be induced in conical-F/S bilayers. When an external bias between the left AF and S is applied, the dynamic part should be added constructively to the static part of the triplet amplitudes [63]. Similar to Ref. [63], long-range spin-triplet correlations may emerge in the AFs under dynamic conditions, which will be investigated in our future work. The magnetoanisotropy of G is quite weak when G_{AR} and G_{ESAR} coexist due to their competing contributions. Conversely, in the presence of anisotropic equal-spin AR alone, significant anisotropic magnetoresistance is observed, suggesting the existence of equal-spin AR and spin-triplet pairing in AF/S junctions.

APPENDIX A: CALCULATION OF THE RETARDED GREEN'S FUNCTION

To study the conventional and equal-spin AR-induced conductance in AF/AF/S junctions, we first introduce the generalized Nambu representation as follows: $\psi_{j_x k_y}^{\pm} = (c_{j_x k_y \uparrow}^{A+}, c_{j_x k_y \uparrow}^{B+}, c_{j_x k_y \downarrow}^{A+}, c_{j_x k_y \downarrow}^{B+}, c_{j_x -k_y \downarrow}^A, c_{j_x -k_y \downarrow}^B, c_{j_x -k_y \uparrow}^A, c_{j_x -k_y \uparrow}^B)$. The Hamiltonian (2) can be rewritten as

$$H = \sum_{j_x k_y} (\psi_{j_x k_y}^+ H_{00} \psi_{j_x k_y} + \psi_{j_x k_y}^+ H_{01} \psi_{j_x + 1 k_y} + \psi_{j_x + 1 k_y}^+ H_{10} \psi_{j_x k_y}), \quad (\text{A1})$$

where for the AFs we introduce the terms

$$H_e = \begin{pmatrix} x - U_{j_x} & -t e^{i k_y a} & -\Delta_{\text{AF}} \sin \alpha & 0 \\ -t e^{-i k_y a} & -x - U_{j_x} & 0 & \Delta_{\text{AF}} \sin \alpha \\ -\Delta_{\text{AF}} \sin \alpha & 0 & y - U_{j_x} & -t e^{i k_y a} \\ 0 & \Delta_{\text{AF}} \sin \alpha & -t e^{-i k_y a} & -y - U_{j_x} \end{pmatrix}, \quad (\text{A2})$$

$$H_h = \begin{pmatrix} -y + U_{j_x} & t e^{i k_y a} & \Delta_{\text{AF}} \sin \alpha & 0 \\ t e^{-i k_y a} & y + U_{j_x} & 0 & -\Delta_{\text{AF}} \sin \alpha \\ \Delta_{\text{AF}} \sin \alpha & 0 & -x + U_{j_x} & t e^{i k_y a} \\ 0 & -\Delta_{\text{AF}} \sin \alpha & t e^{-i k_y a} & x + U_{j_x} \end{pmatrix}. \quad (\text{A3})$$

By using H_{00} and H_{01} , H_{00} can be defined as

$$H_{00} = \begin{pmatrix} H_e & \mathbf{0} \\ \mathbf{0} & H_h \end{pmatrix}. \quad (\text{A4})$$

H_{01} can be expressed as

$$H_{01} = t e^{-\frac{i}{2} k_y a} \begin{pmatrix} -\sigma_0 \otimes \sigma_x & \mathbf{0} \\ \mathbf{0} & \sigma_0 \otimes \sigma_x \end{pmatrix} \quad (\text{A5})$$

with $H_{10} = H_{01}^+$. We define $x = \Delta - \Delta_{\text{AF}} \cos \alpha$ and $y = \Delta + \Delta_{\text{AF}} \cos \alpha$. Δ in the left (central) AF is set as $\Delta_{L(c)}$. U_{j_x} represents the electrostatic potential, with $U_{j_x} = U(eV_g)$ for the left (central) AF. α is set to zero for the left AF. In Eqs. (A4) and (A5), $\mathbf{0}$ is a 4×4 zero matrix. For the S, we assume $x = y = 0$ and $U_{j_x} = \mu_s$ in Eqs. (A2) and (A3), and $V = \Delta_0 \sigma_z \otimes \sigma_0$ and H_{00} is

$$H_{00} = \begin{pmatrix} H_e & V \\ V & H_h \end{pmatrix}. \quad (\text{A6})$$

The retarded Green's function of the central AF is determined by

$$G^r = \left[(E + i\eta)I - H_c - \sum_L^r - \sum_R^r \right]^{-1}. \quad (\text{A7})$$

Here, G^r is an $8N_x \times 8N_x$ matrix, and H_c is the Hamiltonian of the central AF with a unit matrix I , as determined from Eq. (A1). $\sum_{L(R)}^r$ represents the self-energy due to the coupling between the central AF and the AF (S) lead. As an example, considering a short central AF with $N_x = 4$, the retarded function and the self-energies would be 32×32 matrices. \sum_L^r and \sum_R^r can be expressed as

$$\sum_L^r = \begin{pmatrix} \sum_{L0}^r & \mathbf{0} & \mathbf{0} & \mathbf{0} \\ \mathbf{0} & \mathbf{0} & \mathbf{0} & \mathbf{0} \\ \mathbf{0} & \mathbf{0} & \mathbf{0} & \mathbf{0} \\ \mathbf{0} & \mathbf{0} & \mathbf{0} & \mathbf{0} \end{pmatrix}, \quad (\text{A8})$$

$$\sum_R^r = \begin{pmatrix} \mathbf{0} & \mathbf{0} & \mathbf{0} & \mathbf{0} \\ \mathbf{0} & \mathbf{0} & \mathbf{0} & \mathbf{0} \\ \mathbf{0} & \mathbf{0} & \mathbf{0} & \mathbf{0} \\ \mathbf{0} & \mathbf{0} & \mathbf{0} & \sum_{R0}^r \end{pmatrix}. \quad (\text{A9})$$

In Eqs. (A8) and (A9), $\mathbf{0}$ is an 8×8 zero matrix. $\sum_{L(R)0}^r$ is defined as $\sum_{L(R)0}^r = H_{cL(R)} g_{L(R)}^r H_{L(R)c}$, where $H_{cL(R)}$ ($H_{L(R)c}$) represents the coupling matrix between the left (right) lead and the central AF. The surface retarded Green's functions of the left and right leads, denoted as g_L^r and g_R^r , can be calculated numerically [68,69]. The linewidth function for the left (right) lead is given by $\Gamma_{L(R)} = i(\sum_{L(R)}^r - \sum_{L(R)}^+)$. By using the relation $G^a = G^{r+}$, we can obtain the advanced Green function G^a . Once we have obtained the retarded (advanced) Green's function of the central AF and the linewidth function, we can use Eqs. (5)–(7) to calculate the conductance G and the conventional and equal-spin AR coefficients $T_{\text{AR}\sigma\bar{\sigma}}$ and $T_{\text{AR}\sigma\sigma}$, respectively.

APPENDIX B: SPIN-SINGLET AND SPIN-TRIPLET PAIRING CORRELATIONS

To analyze spin-singlet and spin-triplet pairings, superconducting pairing correlations can be determined using anomalous electron-hole Green's function components. We define the retarded Green's function in the Nambu basis as follows:

$$G^r = [(\omega + i\eta)I - H]^{-1}. \quad (\text{B1})$$

ω denotes the frequency, and the Hamiltonian H can be determined from Eq. (2). We assume that the size of the device is finite along the x direction. The component

G_{eh}^r , defined in Eq. (8) in the main text, can be obtained from Eq. (B1). This component is used to calculate the pairing correlations at site j_x . In the Nambu basis, the spin-singlet pairing correlation f_0 and the spin-triplet pairing correlation with $S_z = 0$ f_3 are given by $f_0 = \frac{1}{W} \sum_{k_y} [(G_{eh}^r)_{11} + (G_{eh}^r)_{22} - (G_{eh}^r)_{33} - (G_{eh}^r)_{44}]$ and $f_3 = \frac{1}{W} \sum_{k_y} [(G_{eh}^r)_{11} + (G_{eh}^r)_{22} + (G_{eh}^r)_{33} + (G_{eh}^r)_{44}]$, respectively. $f_{\uparrow\uparrow}$ and $f_{\downarrow\downarrow}$ are given by $f_{\uparrow\uparrow} = \frac{1}{W} \sum_{k_y} [(G_{eh}^r)_{13} + (G_{eh}^r)_{24}]$

and $f_{\downarrow\downarrow} = \frac{1}{W} \sum_{k_y} [(G_{eh}^r)_{31} + (G_{eh}^r)_{42}]$. We focus specifically on intrasublattice pairing correlations, without considering intersublattice pairing correlations [70]. It is important to note that when dealing with negative frequency ($\omega < 0$), the advanced Green's function should be used instead of the retarded Green's function. According to Fermi-Dirac statistics, f_0 is an even function of the frequency, while the other pairing correlations are odd functions of the frequency.

-
- [1] A. F. Andreev, *J. Exp. Theor. Phys.* **19**, 1228 (1964).
[2] M. Tinkham, *Introduction to Superconductivity* (Dover, Mineola, NY, 2004).
[3] G. Deutscher, *Rev. Mod. Phys.* **77**, 109 (2005).
[4] C. W. J. Beenakker, *Rev. Mod. Phys.* **80**, 1337 (2008).
[5] R. J. Soulen Jr., J. M. Byers, M. S. Osofsky, B. Nadgorny, T. Ambrose, S. F. Cheng, P. R. Broussard, C. T. Tanaka, J. Nowak, J. S. Moodera, A. Barry, and J. M. D. Coey, *Science* **282**, 85 (1998); R. J. Soulen Jr., M. S. Osofsky, B. Nadgorny, T. Ambrose, P. Broussard, S. F. Cheng, J. Byers, C. T. Tanaka, J. Nowack, J. S. Moodera, G. Laprade, A. Barry, and M. D. Coey, *J. Appl. Phys.* **85**, 4589 (1999).
[6] J. Linder and A. Sudbø, *Phys. Rev. B* **75**, 134509 (2007).
[7] C. D. Feng, Z. M. Zheng, R. Shen, B. Wang, and D. Y. Xing, *Phys. Rev. B* **81**, 224510 (2010).
[8] Y. Wei, T. Liu, C. Huang, Y. C. Tao, and F. Qi, *Phys. Rev. Res.* **3**, 033131 (2021).
[9] C.-T. Wu, O. T. Valls, and K. Halterman, *Phys. Rev. B* **90**, 054523 (2014).
[10] E. Moen and O. T. Valls, *Phys. Rev. B* **95**, 054503 (2017).
[11] A. Costa and J. Fabian, *Phys. Rev. B* **104**, 174504 (2021).
[12] R. Cai, Y. Yao, P. Lv, Y. Ma, W. Xing, B. Li, Y. Ji, H. Zhou, C. Shen, S. Jia, X. C. Xie, I. Žutić, Q.-F. Sun, and W. Han, *Nat. Commun.* **12**, 6725 (2021).
[13] R. Beiranvand, H. Hamzehpour, and M. Alidoust, *Phys. Rev. B* **94**, 125415 (2016); **96**, 161403(R) (2017).
[14] Z. P. Niu, *Europhys. Lett.* **100**, 17012 (2012).
[15] R. Cai, I. Žutić, and W. Han, *Adv. Quantum Technol.* **6**, 2200080 (2023).
[16] M. Eschrig, *Rep. Prog. Phys.* **78**, 104501 (2015); *Phys. Today* **64**, 43 (2011).
[17] F. S. Bergeret, A. F. Volkov, and K. B. Efetov, *Rev. Mod. Phys.* **77**, 1321 (2005).
[18] M. Eschrig, J. Kopu, J. C. Cuevas, and G. Schön, *Phys. Rev. Lett.* **90**, 137003 (2003).
[19] F. S. Bergeret, A. F. Volkov, and K. B. Efetov, *Phys. Rev. Lett.* **86**, 4096 (2001).
[20] A. F. Volkov, F. S. Bergeret, and K. B. Efetov, *Phys. Rev. Lett.* **90**, 117006 (2003).
[21] R. S. Keizer, S. T. B. Goennenwein, T. M. Klapwijk, G. Miao, G. Xiao, and A. Gupta, *Nature (London)* **439**, 825 (2006).
[22] M. S. Anwar, F. Czeschka, M. Hesselberth, M. Porcu, and J. Aarts, *Phys. Rev. B* **82**, 100501(R) (2010).
[23] A. Singh, C. Jansen, K. Lahabi, and J. Aarts, *Phys. Rev. X* **6**, 041012 (2016).
[24] J. W. A. Robinson, J. D. S. Witt, and M. G. Blamire, *Science* **329**, 59 (2010).
[25] A. Di Bernardo, Z. Salman, X. L. Wang, M. Amado, M. Egilmez, M. G. Flokstra, A. Suter, S. L. Lee, J. H. Zhao, T. Prokscha, E. Morenzoni, M. G. Blamire, J. Linder, and J. W. A. Robinson, *Phys. Rev. X* **5**, 041021 (2015).
[26] A. Di Bernardo, S. Diesch, Y. Gu, J. Linder, E. Scheer, M. G. Blamire, and J. W. A. Robinson, *Nat. Commun.* **6**, 8053 (2015).
[27] M. S. Anwar, M. Veldhorst, A. Brinkman, and J. Aarts, *Appl. Phys. Lett.* **100**, 052602 (2012).
[28] D. Sanchez-Manzano, S. Mesoraca, F. A. Cuellar, M. Cabero, V. Rouco, G. Orfila, X. Palermo, A. Balan, L. Marcano, A. Sander, M. Rocci, J. Garcia-Barriocanal, F. Gallego, J. Tornos, A. Rivera, F. Mompean, M. Garcia-Hernandez, J. M. Gonzalez-Calbet, C. Leon, S. Valencia *et al.*, *Nat. Mater.* **21**, 188 (2022).
[29] A. Singh, S. Voltan, K. Lahabi, and J. Aarts, *Phys. Rev. X* **5**, 021019 (2015).
[30] Y. V. Fominov, A. A. Golubov, and M. Yu. Kupriyanov, *JETP Lett.* **77**, 510 (2003).
[31] A. Srivastava, L. A. B. Olde Olthof, A. Di Bernardo, S. Komori, M. Amado, C. Palomares-Garcia, M. Alidoust, K. Halterman, M. G. Blamire, and J. W. A. Robinson, *Phys. Rev. Appl.* **8**, 044008 (2017).
[32] K. Halterman and M. Alidoust, *Phys. Rev. B* **94**, 064503 (2016).
[33] A. Spuri, D. Nikolić, S. Chakraborty, M. Klang, H. Alpern, O. Millo, H. Steinberg, W. Belzig, E. Scheer, and A. Di Bernardo, *Phys. Rev. Res.* **6**, L012046 (2024).
[34] Y. Kalcheim, O. Millo, A. Di Bernardo, A. Pal, and J. W. A. Robinson, *Phys. Rev. B* **92**, 060501(R) (2015).
[35] M. Alidoust, K. Halterman, and O. T. Valls, *Phys. Rev. B* **92**, 014508 (2015).
[36] M. Alidoust, A. Zyuzin, and K. Halterman, *Phys. Rev. B* **95**, 045115 (2017).
[37] L. Kuerten, C. Richter, N. Mohanta, T. Kopp, A. Kampf, J. Mannhart, and H. Boschker, *Phys. Rev. B* **96**, 014513 (2017).
[38] S. Diesch, P. Machon, M. Wolz, C. Stürgers, D. Beckmann, W. Belzig, and E. Scheer, *Nat. Commun.* **9**, 5248 (2018).
[39] X. Zhou, M. Lan, Y. Ye, Y. Feng, X. Zhai, L. Gong, H. Wang, and J. Zhao, and Y. Xu, *Europhys. Lett.* **125**, 37001 (2019).
[40] E. H. Fyhn, A. Brataas, A. Qaiumzadeh, and J. Linder, *Phys. Rev. Lett.* **131**, 076001 (2023).
[41] K.-R. Jeon, B. K. Hazra, K. Cho, A. Chakraborty, J.-C. Jeon, H. Han, H. L. Meyerheim, T. Kontos, and S. S. P. Parkin, *Nat. Mater.* **20**, 1358 (2021); K.-R. Jeon, B. K. Hazra, J.-K. Kim, J.-C. Jeon, H. Han, H. L. Meyerheim, T. Kontos, A. Cottet, and S. S. P. Parkin, *Nat. Nanotechnol.* **18**, 747 (2023).
[42] M. Ezawa, *Phys. Rev. Lett.* **114**, 056403 (2015).
[43] W.-T. Lu and Q.-F. Sun, *Phys. Rev. B* **104**, 045418 (2021).
[44] M. F. Jakobsen, A. Brataas, and A. Qaiumzadeh, *Phys. Rev. Lett.* **127**, 017701 (2021).
[45] W. Yan, W. Zeng, Y. Huang, and R. Shen, *Eur. Phys. J. B* **97**, 4 (2024).
[46] Z. P. Niu and Y. M. Zhang, *J. Phys. D* **56**, 435303 (2023).

- [47] M. F. Jakobsen, K. B. Naess, P. Dutta, A. Brataas, and A. Qaiumzadeh, *Phys. Rev. B* **102**, 140504(R) (2020).
- [48] B. M. Andersen, I. V. Bobkova, P. J. Hirschfeld, and Y. S. Barash, *Phys. Rev. B* **72**, 184510 (2005).
- [49] B. M. Andersen and P. Hedegård, *Phys. Rev. B* **66**, 104515 (2002).
- [50] I. V. Bobkova, P. J. Hirschfeld, and Y. S. Barash, *Phys. Rev. Lett.* **94**, 037005 (2005).
- [51] B. M. Andersen, I. V. Bobkova, P. J. Hirschfeld, and Y. S. Barash, *Phys. Rev. Lett.* **96**, 117005 (2006).
- [52] B. M. Andersen, Y. S. Barash, S. Graser, and P. J. Hirschfeld, *Phys. Rev. B* **77**, 054501 (2008).
- [53] D. S. Rabinovich, I. V. Bobkova, and A. M. Bobkov, *Phys. Rev. Res.* **1**, 033095 (2019).
- [54] L. Bulaevskii, R. Eneias, and A. Ferraz, *Phys. Rev. B* **95**, 104513 (2017).
- [55] H. Enoksen, J. Linder, and A. Sudbø, *Phys. Rev. B* **88**, 214512 (2013).
- [56] C. Bell, E. J. Tarte, G. Burnell, C. W. Leung, D.-J. Kang, and M. G. Blamire, *Phys. Rev. B* **68**, 144517 (2003).
- [57] P. Komissinskiy, G. A. Ovsyannikov, I. V. Borisenko, Y. V. Kislinskii, K. Y. Constantinian, A. V. Zaitsev, and D. Winkler, *Phys. Rev. Lett.* **99**, 017004 (2007).
- [58] W. Du, R. Peng, Z. He, Y. Dai, B. Huang, and Y. Ma, *npj 2D Mater. Appl.* **6**, 11 (2022).
- [59] M. Luo, *Phys. Rev. B* **99**, 165407 (2019).
- [60] Q.-F. Liang, L.-H. Wu, and X. Hu, *New J. Phys.* **15**, 063031 (2013).
- [61] Y.-X. Dai, Y. Mao, and Q.-F. Sun, *Phys. Rev. B* **106**, 184513 (2022).
- [62] J. Wang, L. Zhang, and K. S. Chan, *Phys. Rev. B* **83**, 125425 (2011); F. Qi, J. Cao, and G. Jin, *ibid.* **98**, 045422 (2018).
- [63] C.-T. Wu and K. Halterman, *Phys. Rev. B* **98**, 054518 (2018).
- [64] C.-T. Wu, O. T. Valls, and K. Halterman, *Phys. Rev. B* **86**, 184517 (2012).
- [65] J. Cayao, C. Triola, and A. M. Black-Schaffer, *Eur. Phys. J. Spec. Top.* **229**, 545 (2020).
- [66] P. Dutta and A. M. Black-Schaffer, *Phys. Rev. B* **100**, 104511 (2019).
- [67] S. Pal and C. Benjamin, *Phys. Rev. B* **104**, 054519 (2021).
- [68] D. H. Lee and J. D. Joannopoulos, *Phys. Rev. B* **23**, 4997 (1981).
- [69] M. L. Sancho, J. L. Sancho, and J. Rubio, *J. Phys. F* **14**, 1205 (1984).
- [70] S. Tamura, S. Nakosai, A. M. Black-Schaffer, Y. Tanaka, and J. Cayao, *Phys. Rev. B* **101**, 214507 (2020).